Radboud Repository

Radboud University Nijmegen

PDF hosted at the Radboud Repository of the Radboud University Nijmegen

The following full text is a publisher's version.

For additional information about this publication click this link.
http://hdl.handle.net/2066/208877

Please be advised that this information was generated on 2019-12-04 and may be subject to change.

Monthly Notices of the ROYAL ASTRONOMICAL SOCIETY
MNRAS **489,** 4111–4124 (2019) doi:10.1093/mnras/stz2333

Outflowing gas in a compact ionization cone in the Seyfert 2 galaxy ESO 153-G20

Pamela Soto-Pinto,[1★] Neil M. Nagar,[1★] Carolina Finlez,[1] Venkatessh Ramakrishnan,[1] Dania Muñoz-Vergara,[1,2] Roy Slater,[3] Pedro K. Humire,[1] Thaisa Storchi-Bergmann,[4] Davide Lena,[5,6] Steven B. Kraemer,[7] Travis C. Fischer,[8] Henrique R. Schmitt,[9] Rogemar A. Riffel,[10] Allan Schnorr-Müller,[4] Andrew Robinson,[11] D. Michael Crenshaw[12] and Martin S. Elvis[13]

[1]*Departamento de Astronomía, Universidad de Concepción, Casilla 160-C, Concepción, Chile*
[2]*Departamento de Física y Astronomía, Universidad de La Serena, Av. Juan Cisternas 1200, La Serena, Chile*
[3]*Dirección de Formación General, Facultad de Educación y Cs. Sociales, Universidad Andres Bello, Sede Concepción, Autopista Concepción-Talcahuano 7100, Talcahuano, Chile*
[4]*Instituto de Física, CP 15015, Universidade Federal do Rio Grande do Sul, 91501-970, Porto Alegre, RS, Brazil*
[5]*SRON, Netherlands Institute for Space Research, Sorbonnelaan 2, NL3584 CA Utrecht, the Netherlands*
[6]*Department of Astrophysics/IMAPP, Radboud University, Nijmegen, PO Box 9010, NL-6500 GL Nijmegen, the Netherlands*
[7]*Institute for Astrophysics and Computational Sciences, Department of Physics, The Catholic University of America, Washington, DC 20064, USA*
[8]*Astrophysics Science Division, Goddard Space Flight Center, Code 665, Greenbelt, MD 20771, USA*
[9]*Naval Research Laboratory, 4555 Overlook Avenue, SW, Washington, DC 20375, USA*
[10]*Universidade Federal de Santa María, Departamento de Física, Centro de Ciencias Naturais e Exatas, 97105-900, Santa Maria, RS, Brazil*
[11]*Department of Physics, Rochester Institute of Technology, 84 Lomb Memorial Drive, Rochester, NY 14623, USA*
[12]*Department of Physics and Astronomy, Georgia State University, Astronomy Offices, 25 Park Place, Suite 605, Atlanta, GA 30303, USA*
[13]*Harvard-Smithsonian Center for Astrophysics 60 Garden St., ms.6, Cambridge, MA 02138 USA*

Accepted 2019 August 16. Received 2019 August 13; in original form 2018 March 28

ABSTRACT

We present two-dimensional ionized gas and stellar kinematics in the inner 1.4 × 1.9 kpc^2 of the Seyfert 2 galaxy ESO 153-G20 obtained with the Gemini-South/Gemini multi-object spectrograph integral field unit (GMOS-IFU) at a spatial resolution of ∼250 pc and spectral resolution of 36 km s^{-1}. Strong [O III], Hα, [N II] and [S II] emission lines are detected over the entire field of view. The stellar kinematics trace circular rotation with a projected velocity amplitude of ±96 km s^{-1}, a kinematic major axis in position angle of 11°, and an average velocity dispersion of 123 km s^{-1}. To analyse the gas kinematics, we used aperture spectra, position–velocity diagrams and single/double Gaussian fits to the emission lines. All lines show two clear kinematic components: a rotating component that follows the stellar kinematics, and a larger-dispersion component, close to the systemic velocity (from which most of the [O III] emission comes), mainly detected to the south-west. We interpret this second component as gas outflowing at ∼400 km s^{-1} in a compact (300 pc) ionization cone with a half-opening angle ≤40°. The counter-cone is probably obscured behind a dust lane. We estimate a mass outflow rate of 1.1 M$_\odot$ yr^{-1}, 200 times larger than the estimated accretion rate on to the supermassive black hole, and a kinetic to radiative power ratio of 1.7 × 10^{-3}. Bar-induced perturbations probably explain the remaining disturbances observed in the velocity field of the rotating gas component.

Key words: galaxies: active – galaxies: individual: ESO 153-G20 – galaxies: kinematics and dynamics – galaxies: nuclei – galaxies: Seyfert.

★ E-mail: pame.sotopinto@gmail.com (PS-P); nagar@astro-udec.cl (NMN)

© 2019 The Author(s)
Published by Oxford University Press on behalf of the Royal Astronomical Society

Downloaded from https://academic.oup.com/mnras/article-abstract/489/3/4111/5571294 by Radboud University user on 23 October 2019

1 INTRODUCTION

Investigations into the gas kinematics in nearby low-ionization nuclear emission-line region (LINER)/Seyfert galaxies can be used to search for signatures of gas inflows and/or outflows to/from the nucleus (e.g. Fathi et al. 2006; Storchi-Bergmann et al. 2007; Davies et al. 2009; Rosario et al. 2010; Schnorr Müller et al. 2011; Combes et al. 2013; García-Burillo et al. 2015; Lena et al. 2015; García-Burillo et al. 2017); to allow the determination of the mass of the central region in a galaxy (e.g. Kormendy & Ho 2013); and to study the stellar population in the central region of a galaxy after decoupling the gas from the stellar kinematics (Sarzi et al. 2005; Repetto et al. 2017).

It is now widely accepted that the radiation emitted by an active galactic nucleus (AGN) is the result of the accretion of gas on to a supermassive black hole (hereafter SMBH) (Lynden-Bell 1969; Begelman, Blandford & Rees 1984). This has motivated the search for signatures, such as inflows and outflows, of the mechanisms responsible for transferring mass from galactic scales down to nuclear scales to feed the SMBH. Simões Lopes et al. (2007) found that there is a marked difference in the dust and gas content in the nuclei of early-type active galaxies as compared with non-active ones: while the former always have dusty structures, in the form of spirals and filaments at scales of hundreds of parsecs, only 25 per cent of non-active galaxies have such structures. This indicates that a reservoir of gas and dust is a necessary condition for nuclear activity and also suggests that the dusty structures are tracers of feeding channels to the AGN.

Simulations and theoretical studies have shown that non-axisymmetric potentials efficiently promote gas inflow towards the inner regions of galaxies (Shlosman, Begelman & Frank 1990; Englmaier & Shlosman 2004; Knapen 2005; Emsellem et al. 2006), where structures such as nuclear bars, spiral arms and small-scale discs are commonly observed (e.g. Erwin & Sparke 1999).

In order to better understand the extent, geometry, kinematics and energetics of the narrow-line region (NLR) on $\leq$100-pc scales in a well-defined sample of nearby AGNs, we have been pursuing high-resolution integral field unit (IFU) observations of ($\sim$30) Seyfert galaxies from the *Hubble Space Telescope* (*HST*) [O III] Snapshot Survey of Schmitt et al. (2003) selected to (a) have NLRs that extend beyond $\sim$1 arcsec from the nucleus, and (b) cover the full range (39 $\leq$ log (L[O III]) $\leq$ 42 erg s^{-1}) of AGN luminosities of the sample. Results on individual or subsets of galaxies can be found in Schnorr-Müller et al. (2014a,b), Riffel, Storchi-Bergmann & Riffel (2015), Lena et al. (2016), Finlez et al. (2018), Humire et al. (2018), Freitas et al. (2018), Slater et al. (2019), Muñoz-Vergara et al. (2019) and Ramakrishnan et al. (2019), and overall results of the study will be published on completion of the sample. As part of this study, we observed ESO 153-G20 with the IFU of the Gemini multi-object spectrograph (GMOS-IFU). The results and analysis are sufficiently detailed (and no previous kinematic study of this galaxy is available in the literature) that we present them independently in this work.

ESO153-G20 is a nearby SBab galaxy harbouring a Seyfert 2 nucleus (RC3: de Vaucouleurs et al. 1991; de Grijp, Lub & Miley 1987); it is located at a distance of 79.4 $\pm$ 5.6 Mpc (from NED,[1] derived assuming a redshift of 0.019737 and H_0 = 73.0 km s^{-1} Mpc^{-1}), corresponding to a scale of 385 pc arcsec^{-1} and a heliocentric velocity of 5917 $\pm$ 28 km s^{-1} (da Costa et al. 1991). Many extremely different major axis position angles (hereafter PAs) have been suggested for this object, from 14° (Lauberts & Valentijn 1989), through 125° (Skrutskie et al. 2006, hereafter 2MASS) to 164° (Paturel et al. 2003, hereafter HYPERLEDA). This variation is primarily a result of the presence of rings, which change the perspective of this object depending on the observation band used. For example, Schmitt & Kinney (2000) found PAs of 8° and −50° using images taken in the *I* and *B* band, respectively. These rings have been relatively well characterized in Buta & Crocker (1991, 1993) and in Buta (1995). In these works, the authors determine that ESO153-G20 is a classical example of a '2 + 2' spiral arm multiplicity, namely two main arms and two secondary ones, that shows a very open inner pseudo-ring (rs) around a prominent bar, and is also one of the best cases of a Type I Schwarz outer pseudo-ring (R'$_1$).

The listed diameters of ESO 153-G20 vary from 93 to 114 arcsec (RC3; Lauberts 1982; Lauberts & Valentijn 1989; 2MASS), using a reference level of $\sim$25.0 *B*-mag arcsec^{-2} in the case of the former three works, and a reference level of 20.0 *K*-mag arcsec^{-2} in the case of 2MASS. For the minor axis, we found only one determination, of 72 arcsec by Lauberts (1982), using the same reference level of 25.0 *B*-mag arcsec^{-2}. An ellipticity between 0.37 and 0.40 has also been determined by the same authors.

In the *HST* imaging survey of extended [O III] λ5007 emission in Seyferts, Schmitt et al. (2003) found that the bulk of the emission-line region comes from the inner 385 pc and is extended along PA = −100°. These authors interpret this as an ionization cone to the south-west with a half-opening angle of 40°. They also found diffuse emission in a region of $\sim$1.85 × 2.65 arcsec^2 around the nucleus, with the major axis at PA = −10°.

The present paper is organized as follows. Section 2 describes the observations and data reduction. Section 3 presents the procedures used for the analysis of the data and the subsequent results. Section 4 briefly discusses our results, and Section 5 presents our conclusions.

2 OBSERVATIONS AND DATA REDUCTION

The observations were obtained with the GMOS-IFU (Hook et al. 2004; Allington-Smith et al. 2002) at the Gemini South Telescope on the night of 2014 October 29 as part of the project GS-2014B-Q-20 (P.I. Nagar). The observations were obtained in 'one-slit' mode and consisted of two IFU fields, covering a field of view (FOV) of 3.5 × 5 arcsec^2 each, and resulting in a total usable coverage of 3.6 × 4.9 arcsec^2 around the nucleus. Two exposures of 900 s each were obtained for each field, slightly shifted spatially and in wavelength coverage, in order to correct for detector defects after combination of the frames. The seeing during the observation was $\sim$0.65 arcsec, as listed in the observation log, and confirmed by measuring the full width at half-maximum (FWHM) of the profiles of four stars in the science acquisition image. This corresponds to a spatial resolution of $\sim$250 pc at the distance of the galaxy.

We used the B600_G5323 grating with a central wavelength of either 5700 or 5750 Å, resulting in a spectral range of 4110–7280 Å, which covers the Hβ, [O III] $\lambda\lambda$4959, 5007, Hα + [N II] $\lambda\lambda$6549, 6583 and [S II] $\lambda\lambda$6717, 6731 emission lines. The wavelength sampling was 0.51 Å per pixel at a spectral resolution of *R* $\sim$ 3550, corresponding to $\sigma_{\rm inst} \approx 36$ km s^{-1}, as measured from the arc spectra.

Data reduction was performed using specific tasks developed for GMOS data in the *gemini.gmos* package as well as generic

[1]The NASA/IPAC Extragalactic Database (NED) is operated by the Jet Propulsion Laboratory, California Institute of Technology, under contract with the National Aeronautics and Space Administration.

Downloaded from https://academic.oup.com/mnras/article-abstract/489/3/4111/5571294 by Radboud University user on 23 October 2019

tasks in PyRAF.[2] The reduction process included bias subtraction, bad-pixel masking, flat-fielding, trimming, wavelength calibration, sky subtraction, relative flux calibration, differential atmospheric refraction correction, building of the data cubes at a sampling of 0.1×0.1 arcsec^2, and finally the alignment and combination of the four data cubes using the PyFU[3] package. We also performed cosmic ray rejection using the Laplacian Cosmic Ray Identification code (L.A.Cosmic) written by van Dokkum, Bloom & Tewes (2012).

Flux calibration was performed using the spectroscopic standard star LTT 2415 ($V = 12.21$), for which fluxes are tabulated every 50 Å (Hamuy et al. 1992, 1994). It was observed in a 600-s exposure on the night of 2014 October 11, with the same instrument setup as for the galaxy. The flux calibration step applies by default an arbitrary scaling of 10^{15} in order to avoid later numerical errors. This factor was considered to give true flux units in our analysis.

Sky subtraction was performed using spectra from the 'Sky' FOV.[4] In Fig. 1, we note a residual Telluric absorption at ∼6870 Å (see spectrum at position 1) that affects the [S II] λ6731 emission line. In order to correct this feature, we created a pseudo-spectrum of the standard star, using the absolute magnitudes on the *V*, *R*, *I*, *J*, *H* and *K* bands and the *imexpr* task from IRAF.[5] The observed spectrum of the standard star was divided by this pseudo-spectrum in order to obtain a 'flat' spectrum that was used to correct for Telluric absorption in each spectrum of the data cube. The result of this process can be observed in the spectra at positions 2 and 3 of Fig. 1. We note that the science and flux calibrator exposures were taken on different nights, and thus the Telluric subtraction is not optimal. This does not change any of our principal science results, as this absorption only affects a small region close to the [S II] lines.

3 RESULTS

Fig. 1 presents an overview of our target galaxy and observations. The upper left panel shows the Gemini GMOS acquisition image of ESO153-G20, where we can observe the spiral arms. The upper right panel shows an image of the inner 8×8 arcsec^2 of the galaxy obtained with the Wide-Field Planetary Camera 2 (WFPC2) through the filter F547M aboard the *HST*. The middle left panel presents a 'structure' map of the same FOV as the WFPC2 image, where the rectangle shows the GMOS FOV of our observations. This structure map was obtained following the process detailed in Pogge & Martini (2002); it was derived using a deconvolved *HST* image, in conjunction with a synthetic point spread function (PSF) produced with the Tiny Tim software (Krist, Hook & Stoehr 2011). In the structure map, we clearly see more dust obscuration to the east, implying that the near side of the galaxy disc is to the east. This interpretation is consistent with the assumption of trailing spiral arms. The red circles plotted on each side of the nucleus will be discussed in Section 4; these correspond to the apertures where we posit a visible ionization cone (south-west) and its corresponding obscured cone (north-east). In the middle right panel, we show the stellar continuum image from Gemini/GMOS-IFU, obtained by integrating the flux within a line-free spectral window from λ5400 to λ5800 Å. The solid line represents the kinematic major axis of the galaxy (PA = 11°), obtained from our analysis of the stellar kinematics (see Section 3.1), and the dashed line represents the minor axis.

In the lower panel of Fig. 1, we present three spectra from the locations marked as 1 (nucleus), 2 (intermediate region) and 3 (boundary region) in the IFU image and extracted using an aperture diameter of 0.4 arcsec (∼154 pc). The position of the stellar kinematic centre was adopted as the nucleus of the galaxy (derived in Section 3.1). We clearly detect strong emission lines – Hβ, [O III] λλ4959, 5007, Hα + [N II] λλ6549, 6583 and [S II] λλ6717, 6731 – in all the spectra. All permitted lines show only 'narrow components' after subtraction of the stellar component (see Section 3.1), consistent with the classification of ESO 153-G20 as a Seyfert 2 galaxy.

3.1 Stellar kinematics

In order to measure the stellar kinematics, we employed the penalized pixel fitting technique (pPXF) (Cappellari & Emsellem 2004; Cappellari 2017) using as template spectra the Medium-resolution Isaac Newton Telescope Library of Empirical Spectra (MILES) Stellar Library (Vazdekis et al. 2010). These models have a spectral resolution of 2.5 Å (FWHM), as estimated in Falcón-Barroso et al. (2011) (or $\sigma_{\rm inst} \sim 64$ km s^{-1}), and cover the range 3525–7500 Å (Sánchez-Blázquez et al. 2006). The final dispersion maps obtained were corrected, in quadrature, for both the mismatch in the spectral resolution of the science spectra and templates, and the intrinsic spectral resolution of the science spectra. To ensure the reliability of the stellar kinematic measurements, the final data cube was spatially binned using the Voronoi binning method (Cappellari & Copin 2003), creating bins with a minimum signal-to-noise ratio (S/N) of 25 per bin.

Before running pPXF, we first identified and masked the spectral regions contaminated by emission lines: this included the lines mentioned in Section 2, with the addition of Hδ, Hγ, He II λ4685, [N I] λλ5198, 5200 and [O I] λλ6300, 6363. The bottom panels of Fig. 1 show examples of observed spectra, the best-fitting stellar template obtained with pPXF, and the corresponding residual (observed − fit). Here, at positions (2) and (3), they correspond to the binned data cube.

The stellar velocity field (v_*) derived from pPXF is shown in the left panel of Fig. 2. There is a clear rotation pattern, reaching projected velocities of ∼96 km s^{-1} within our FOV. The line of nodes is oriented close to the north–south direction, with the north side receding and the south side approaching. Although the major axis is along the shorter side of our FOV, we are still able to obtain reliable results for the kinematics. The stellar velocity dispersion (σ_*), shown in the rightmost panel, varies between 76 and 188 km s^{-1} across the FOV.

We fitted a rotation model to the stellar velocity field, after obtaining the best-fitting systemic velocity of the galaxy ($V_s \approx 5907$ km s^{-1}) and the PA of the kinematic major axis (PA = 11°), measured from north to east, using both *Kinemetry* and *Fit kinematic PA* (Krajnović et al. 2006) IDL routines. For this purpose, we assumed the kinematic centre as the zero-velocity point of the stellar velocity field. If we also assume a spherical potential and circular orbits in a plane, the observed radial velocity at a position (R, ψ) in

[2]PyRAF is a product of the Space Telescope Science Institute, which is operated by AURA for NASA.

[3]Version 0.9 of the PyFU 3D data manipulation package was contributed by James Turner through the Gemini Data Reduction User Forum.

[4]For further details, check the Gemini/GMOS-IFU web page http://www.gemini.edu/sciops/instruments/gmos/integral-field-spectroscopy/basic-design.

[5]IRAF is distributed by the National Optical Astronomy Observatories, which are operated by the Association of Universities for Research in Astronomy, Inc., under cooperative agreement with the National Science Foundation.

Downloaded from https://academic.oup.com/mnras/article-abstract/489/3/4111/5571294 by Radboud University user on 23 October 2019

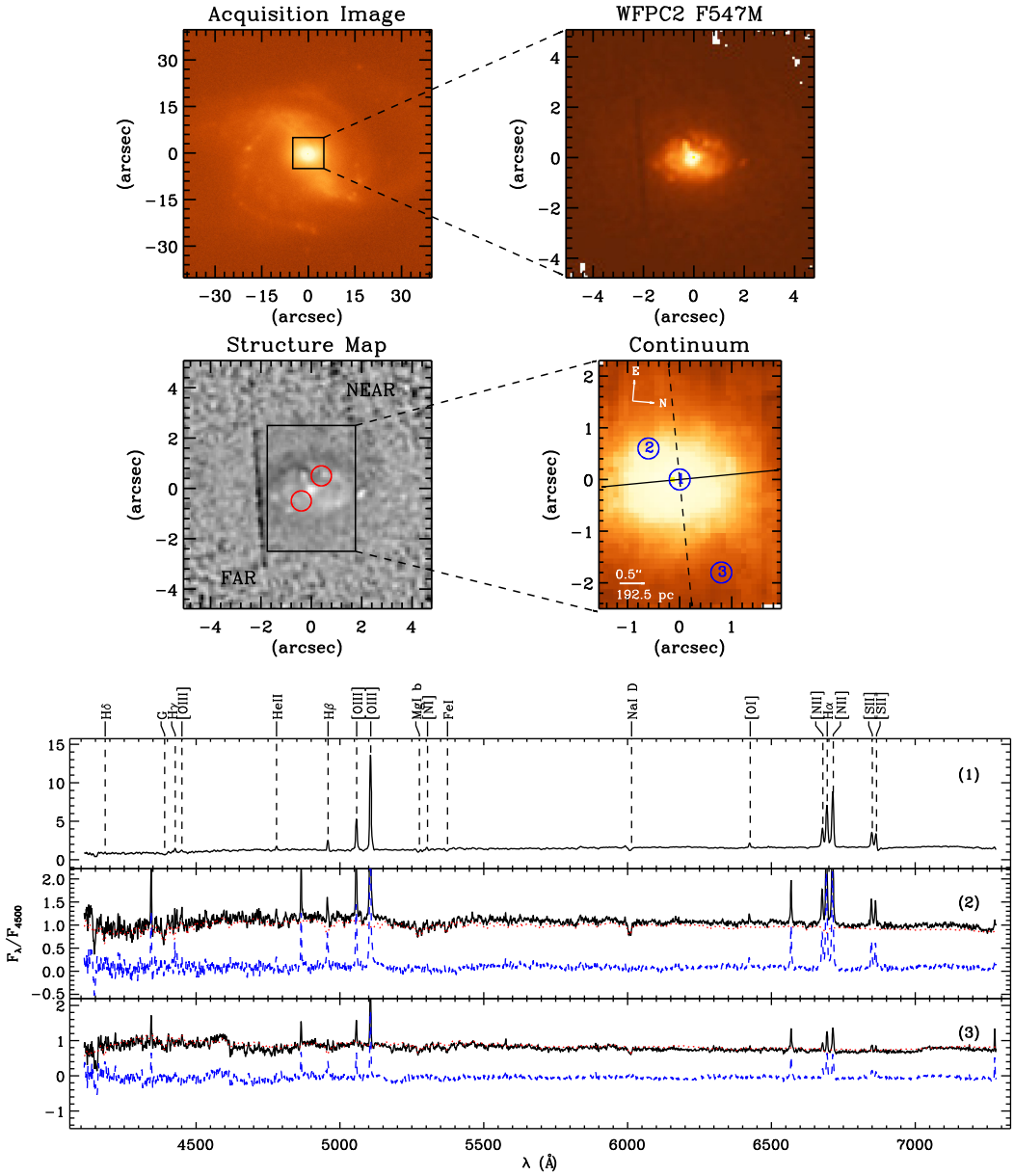

Figure 1. *Top left:* acquisition image from Gemini GMOS. *Top right: HST*-WFPC2 image of the nuclear region marked on the acquisition image. *Middle left:* Structure map of the *HST*-WFPC2 image showing the GMOS FOV. The red circles correspond to the apertures towards which we posit (Section 4) a visible ionization cone (south-west) and its corresponding obscured cone (north-east). *Middle right:* stellar continuum image extracted from the IFU data cube. The solid (dashed) line represents the kinematic major (minor) axis (derived in Section 3.1). *Bottom:* observed-frame spectra (black solid lines) corresponding to the regions marked as (1), (2) and (3) in the continuum image. For regions (2) and (3), we also show the best-fitting stellar spectrum derived by PPXF (red dotted line) and the residual (observed − stellar) spectrum (blue dashed line). All images have the orientation defined by the compass shown in the middle right panel.

the plane of the sky is given by (Bertola et al. 1991):

$$V = V_s + \frac{AR\cos(\psi-\psi_0)\sin(\theta)\cos^p\theta}{\{R^2[\sin^2(\psi-\psi_0)+\cos^2\theta\cos^2(\psi-\psi_0)]+c^2\cos^2\theta\}^{p/2}}. \quad (1)$$

Here, θ is the inclination of the disc (with $\theta = 0$ for a face-on disc); ψ_0 is the position angle of the line of nodes; V_s is the systemic velocity; R is the projected radius from the nucleus; A is the amplitude of the velocity curve; c is the concentration parameter, which indicates at what distance the rotation curve reaches its maximum; and p describes the behaviour of the velocity curve beyond its maximum value (e.g. if it flattens, p=1, or decreases). For galaxies, we expect $1 \leq p \leq 3/2$.

The best-fitting parameters are shown in Table 1, while the second and third panels of Fig. 2 show the best-fitting stellar rotation model and the velocity residual.

3.2 Gas kinematics

3.2.1 Single Gaussian fit

We used the *Profit* IDL routine (Riffel 2010) to fit the strong emission lines with a single Gaussian profile to obtain the emission-line fluxes, centroid velocities and velocity dispersions of the gas. In

Downloaded from https://academic.oup.com/mnras/article-abstract/489/3/4111/5571294 by Radboud University user on 23 October 2019

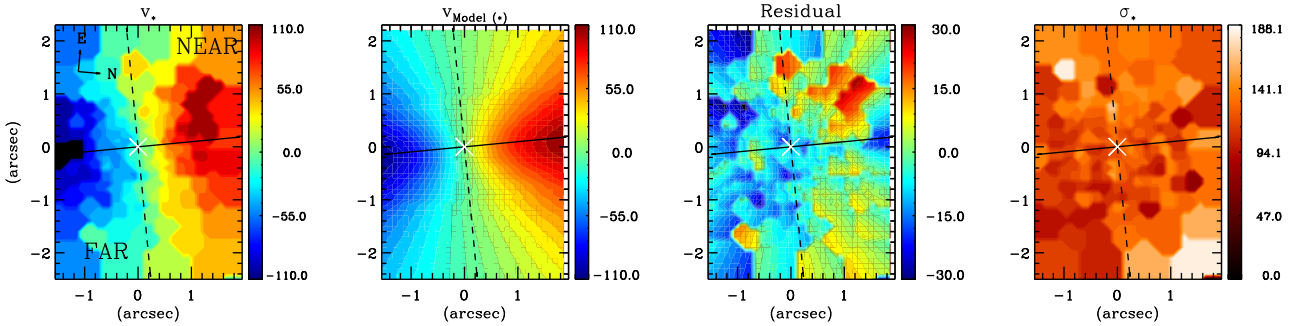

Figure 2. From left to right: observed stellar radial velocity field (km s^{-1}), best-fitting rotation model, residual (observed − model), and stellar velocity dispersion (km s^{-1}). The solid (dashed) lines mark the positions of the kinematic major (minor) axis, and the white cross marks the stellar kinematic centre. Each panel follows the colour bar on its right.

Table 1. Parameters of the best-fitting rotation models.

Parameter	Stars	[N II] λ6583	[N II] 'eye' fit
A (km s^{-1})	145	265	280
c (arcsec)	1.2	3.0	1.2
p	1.0	1.0	1.0
θ (°)	51	51	46
ψ_0 (°)	11	11	11

Notes. Column 1, parameter name (see text for details); column 2, best-fitting parameter values for the stellar velocity field; column 3, values for the [N II] λ6583 velocity field; and column 4, values for the [N II] 'eye' fit.

Fig. 3 we present the integrated flux distributions, velocity fields and dispersion maps of the [O III] λ5007 Å, Hα, Hβ, [N II] λ6583 Å and [S II] λ6716 Å emission lines.

The emission-line fluxes show the highest values within a region with radius ∼1 arcsec (385 pc), centred about 0.25 arcsec to the south-west of the stellar kinematic centre. The flux distribution of the [O III] emission line appears mainly axisymmetric around this centre, but at fainter fluxes it appears to be extended along PA ≈ 110°, close to the value reported by Schmitt et al. (2003) using *HST* imaging. In the case of Hα and Hβ, the distributions appear more symmetric with respect to the nucleus, reaching values of 0.9 and 0.2 ($\times 10^{-15}$ erg cm^{-2} s^{-1}) in an aperture of radius 0.2 arcsec around the centre, respectively. The Hα and Hβ flux distributions seem also to extend more to the north than the [O III] flux distribution, while the [N II] and [S II] distributions seem to be an intermediate between [O III] and Hα, being slightly axisymmetric and showing a slight elongation to the north.

The centroid velocity maps for Hα, Hβ, [N II] and [S II] (second row of Fig. 3) show signatures consistent with rotation in a disc, reaching amplitudes of ∼200 km s^{-1}, but also showing some distortions that are particularly evident in the case of Hα, which shows an S-shaped velocity pattern characteristic of barred disc galaxies (see Section 4). On the other hand, the [O III] emission line shows significantly lower velocities, reaching values of only ∼30 km s^{-1} in the inner 1.5 arcsec. In order to better visualize the large difference in the [O III] kinematics, Fig. 4 plots the change of velocity with radius along the (stellar) kinematic major axis, namely the rotation curve, of all strong emission lines. Here the Hα, [N II] and [S II] emission lines show a radial profile consistent with rotation, while the [O III] emission line is mostly close to zero velocity.

We fitted a Bertola rotation model to the [N II] λ6583 emission-line velocity map, following the same procedure as for the stellar field (Section 3.1). The parameters A, c and p were free, while the inclination and major axis PA were fixed to the values determined from the stellar velocity field best fit. Using the results of the best fit to the emission line as a starting point, we changed all the parameters in order to obtain a model that best fit (by 'eye') the position–velocity diagrams presented in Section 3.2.2. This gave significantly different results because, as mentioned above, the observed gas kinematics appear to show multiple velocity components, so that the velocity field from the single Gaussian fit does not reflect the rotating gas component only. The parameter values of these two Bertola fits to the emission-line kinematics are listed in the third and fourth columns of Table 1.

Fig. 5 shows the rotation models obtained for the stellar and [N II] emission line along with the gas velocity residual (observed − modelled) fields. Both visually and by comparing the rms in the residuals, it is clear that the Hα and [N II] emission lines show velocity fields more in agreement with the [N II] rotation model, while the [O III] emission line velocity field more closely resembles the stellar rotation model.

Velocity dispersion maps of the emission lines, after correcting for the instrumental resolution ($\sigma_{\rm inst} \approx 36$ km s^{-1}), are shown in the third row of Fig. 3. The mean dispersion value seen over all emission lines is ∼90 km s^{-1}. The Hα and Hβ lines show lower dispersions (∼60 km s^{-1}) to the north-east, and higher dispersions to the south-west. The former values are consistent with the dispersion observed in the rotating component of the gas (see Section 3.2.2). The higher dispersions seen to the south-west can be explained by the superposition of rotating gas with an outflow along an ionization cone (Section 4).

Fig. 6 presents maps of the [N II]/Hα, [O III]/Hβ, Hα/Hβ and [S II]6716/6730 line ratios. We also estimated the electron density from the [S II] line ratio in some representative spectra, assuming an electron temperature of 10 000 K (Osterbrock 1989); it is as high as 1200 cm^{-3} at the nucleus and decreases to ∼700 cm^{-3} at 1 arcsec from the nucleus. The [N II]/Hα line ratio has values between 1.0 and1.5 within the inner 1 arcsec, while Hα/Hβ reaches values between 3.9 and 5.2 within the same region. The [O III]/Hβ line ratio varies between 4.6 and 11.0 in the inner 1 arcsec, with a value of 8.4 in the nucleus. These ratios are typical of AGNs rather than of star-forming (H II region) galaxies (Kauffmann et al. 2003; Kewley et al. 2006).

3.2.2 Position–velocity diagrams, line profiles and double Gaussian fits

We made position–velocity (P-V) diagrams for the three strongest emission lines – [O III], Hα and [N II] – in order to better constrain

Downloaded from https://academic.oup.com/mnras/article-abstract/489/3/4111/5571294 by Radboud University user on 23 October 2019

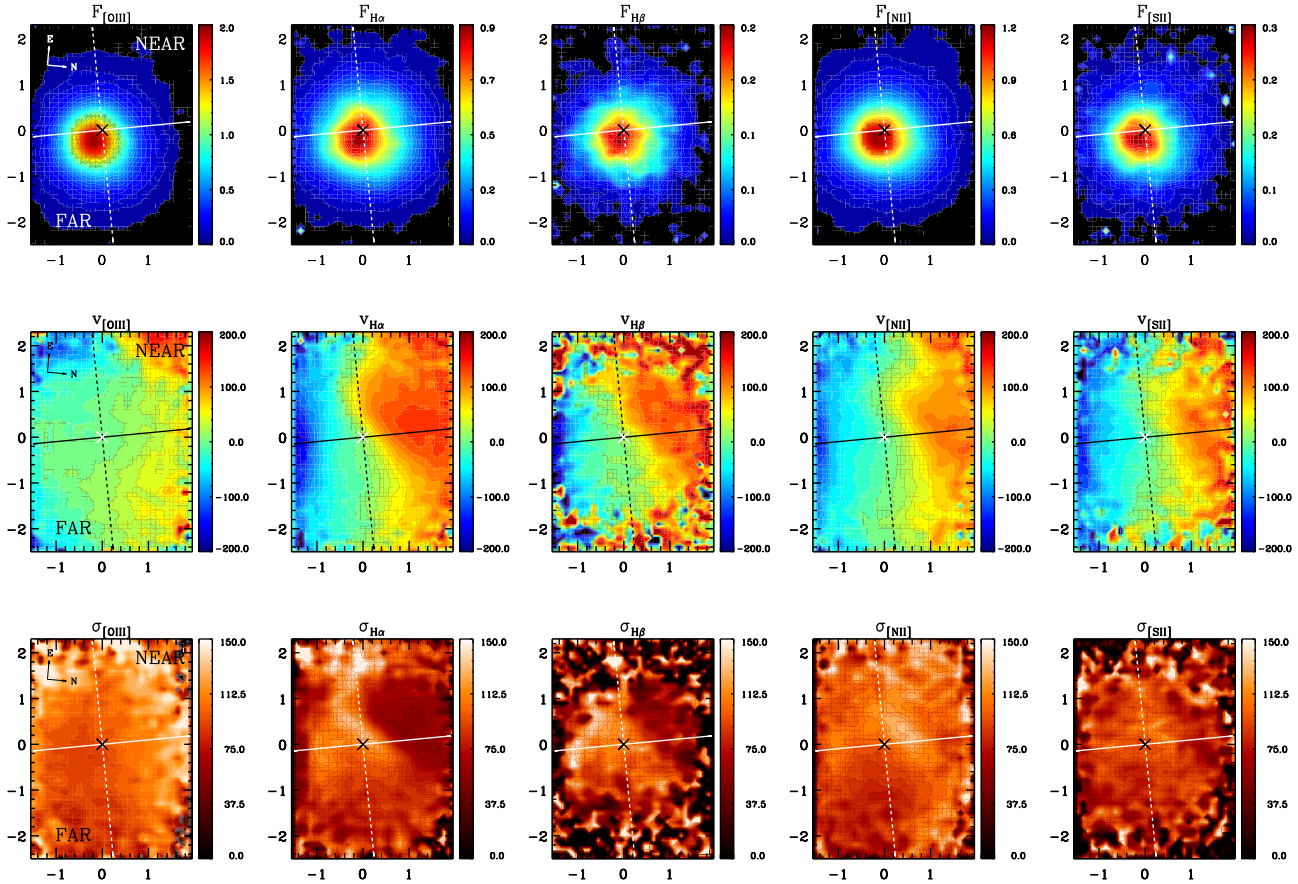

Figure 3. From top to bottom: maps of the integrated fluxes (10^{-15} erg cm^{-2} s^{-1} Å^{-1} arcsec^{-2}), centroid velocities (km s^{-1}) and velocity dispersions (km s^{-1}) derived from the single Gaussian fit to the [O III], Hα, Hβ, [N II] and [S II] emission lines. Each panel follows the colour bar on its right, and the axes (in arcsec) are relative to the stellar kinematic centre, indicated by the intersection of the solid and dashed lines on each map. The solid (dashed) lines indicate the major (minor) axes. The near and far sides of the disc are indicated on the panels in the leftmost column. The zero velocity corresponds to a systemic velocity of 5907 km s^{-1}.

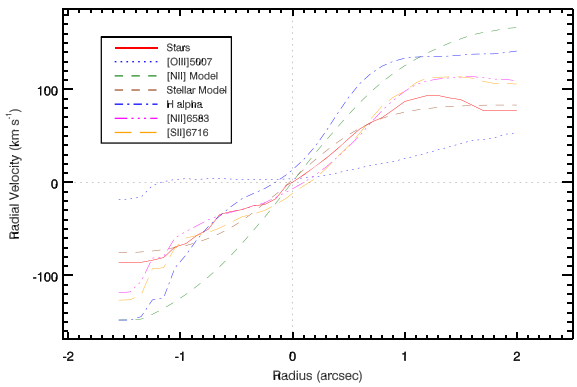

Figure 4. Radial velocity 'rotation curves' along the kinematic major axis (PA $= 11°$) for the stellar velocity field and the strongest emission lines, following the legend in the top left. For emission lines, the velocities are those obtained by the single Gaussian fit. For reference, the best-fitting Bertola stellar rotation model and [N II] rotation model are also shown.

their kinematics. Our analysis used P-V diagrams centred on the stellar kinematic centre, and systemic velocity derived from the best-fitting Bertola model to the stellar velocity field, along 36 different PAs spaced by 5°. Fig. 7 shows the most relevant of these P-V diagrams, including those along the major and minor axes. For a direct comparison, we also overplot the velocities derived from the single-Gaussian fit to the respective emission line, the best-fitting model to the stellar velocity field, the 'by eye' fit to the [N II] (which was obtained by visual fitting to these P-V diagrams), and the 'best' bar perturbation model (see Section 4 for details on the latter). It is clear that the velocities derived from the single Gaussian fit do not represent well the rotating component in the case of Hα and [N II], especially on the blue-shifted side, where the presence of a second lower velocity component is clearly seen. The [N II] 'by eye' model, as mentioned in Section 3.2, is the one that best represents the velocities seen in the Hα and [N II] emission lines in most PAs, although at some PAs it predicts velocities lower than those observed on the red-shifted side (the north-east side of the galaxy). In the case of [O III], the P-V diagrams are completely different: there is some agreement with the predictions of the [N II] model at the faintest contours, but the strongest emission comes from gas with velocities very close to systemic at all PAs and all distances from the nucleus.

To complement the P-V diagrams, in Fig. 8 we show normalized profiles of the [O III], Hα, [N II] and [S II] emission lines, extracted from several 0.2-arcsec-radius apertures distributed over our FOV. These spectra have been continuum-subtracted using the *continuum* task from IRAF. Many apertures show two velocity components, but it is easy to appreciate the difficulty of separating these two components because the width of the non-rotating component is

Downloaded from https://academic.oup.com/mnras/article-abstract/489/3/4111/5571294 by Radboud University user on 23 October 2019

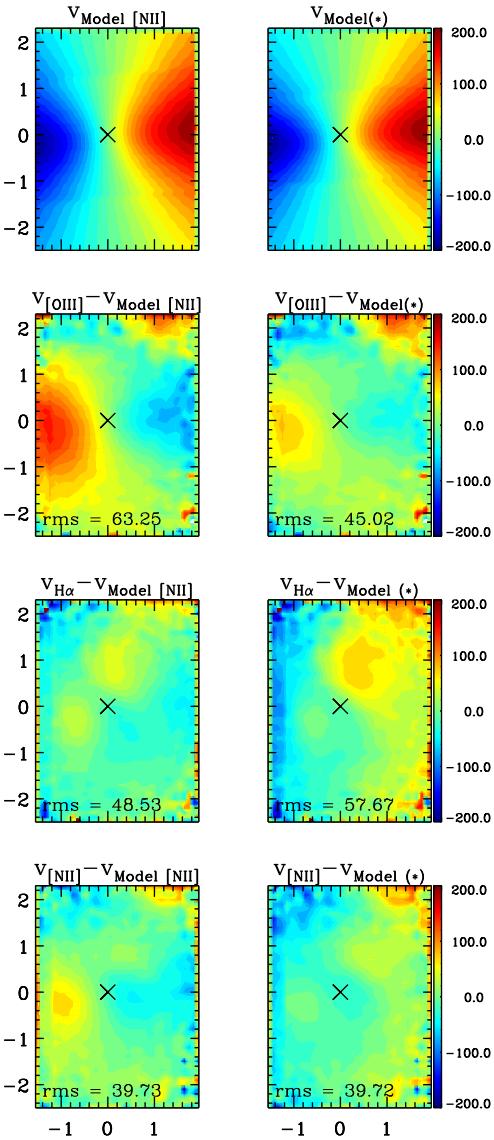

Figure 5. The best-fitting Bertola rotation model for the [N II] and stellar velocity fields (top row), and the velocity residual fields for the [O III], Hα and [N II] emission lines (rows two to four, respectively). The stellar kinematic centre is marked by a black cross, and the axes are in arcseconds. Each row follows the colour bar on its right. Velocity units are in km s^{-1}.

similar to the total velocity variation in our FOV in the rotating component. It is easy to determine that the [O III] profile (solid line) peaks at zero velocity (the galaxy systemic velocity) in all apertures, showing slight wings or a small rotating component in agreement with the model prediction in some of the apertures from the north side. Its mean full width at 10 per cent is ∼490 km s^{-1}, considering the apertures with high S/N. The apertures located along the major axis, and close to it, show that Hα (dot–dashed line) has either two components, or one with a weak wing: one component peaks at zero velocity, in agreement with [O III], and the other one is close to the predicted velocity of the rotation model. The two apertures close to the minor axis show profiles with almost the same behaviour as [O III]. The one to the north-east shows the rotating component in Hα, which corresponds to the red-shifted location in the velocity maps. The [N II] and [S II] lines show, in all apertures, a behaviour intermediate between Hα and [O III], tracing both the rotation and the zero-velocity component.

As clearly demonstrated, a second velocity component is often observed in some of the emission lines. We performed double Gaussian fits to the [O III], Hα and [N II] emission lines, as they have the highest S/Ns. With this approach we obtained the following results.

(i) The flux distributions show, in the case of the [O III] emission line, that the non-rotating component is brighter than the rotating one (a peak value of 1.8×10^{-15} erg cm^{-2} s^{-1} versus a peak value of 0.7×10^{-15} erg cm^{-2} s^{-1}). The flux distribution of the non-rotating component appears symmetric: its flux peaks at a location ∼0.25 arcsec to the south-west from the stellar kinematic centre, and it is extended by ∼0.9 arcsec in FWHM (after deconvolution of the seeing). In the case of Hα, the two velocity components show roughly similar morphologies and intensities, but the rotating component is more extended to the east (the near side of the disc). The location of the flux peak for both components is slightly to the south-west of the kinematic centre. The [N II] line profiles (Fig. 8) are intermediate between those of [O III] and Hα, and thus the flux distributions observed for both components appear to be very symmetric with a slight elongation to the north-east and a peak value of $\sim 0.6 \times 10^{-15}$ erg cm^{-2} s^{-1} located at 0.25 arcsec south-west of the nucleus. In Fig. 9, we plot the flux ratio of the rotating component to the zero-velocity component for [O III] and Hα. In both cases, the greatest values (up to 6 in Hα) are located to the north side of the disc.

(ii) In the velocity fields (not shown), we recover the rotating pattern seen in the single Gaussian fit in Hα (including the S-shape), but now with amplitudes of the order of 100 km s^{-1} and a more symmetric distribution. In the case of [O III], the rotating component is mostly observed to the north, with values close to 100 km s^{-1}, while to the south the velocity amplitudes reach only ∼50 km s^{-1}; we note, however, that the asymmetry is affected by large uncertainties owing to the poorly constrained two-component fits. For the [N II] emission line, the rotating component reaches amplitudes of the order of ∼90 km s^{-1}. The non-rotating component, in all emission lines, shows velocity dispersions of the order of ∼200 km s^{-1} to the south-west, which we will later argue to be due to outflowing gas in an ionization cone. In the opposite direction (north-east), low-velocity dispersions (close to 60 km s^{-1}) are seen. Thus, overall, the second, high velocity-dispersion component centred on zero velocity is primarily detected to the south-west, at a position ∼0.25 arcsec from the kinematic centre, while the emission-line gas to the north-east is predominantly rotating.

Finally, as previously mentioned, the coincidence between the width of the non-rotating component and the total velocity variation in the rotating one did not allow us to perform double Gaussian fits to the Hα and [N II] lines in all the apertures. We thus chose, from Fig. 8, the five apertures where the two components can be easily separated in velocity and then performed a double Gaussian fit to the Hα profile. The results of these double Gaussian fits are used in Section 4 to estimate the gas mass and mass outflow rate. From these fits, we obtain a mean velocity dispersion of $\bar{\sigma} \sim 124$ km s^{-1} for the non-rotating component and of $\bar{\sigma} \sim 60$ km s^{-1} for the rotating component.

3.3 The black hole mass and accretion rate

There are no direct black hole mass measurements for ESO 153-G20. We thus use the relationship of Gültekin et al. (2009) to

Downloaded from https://academic.oup.com/mnras/article-abstract/489/3/4111/5571294 by Radboud University user on 23 October 2019

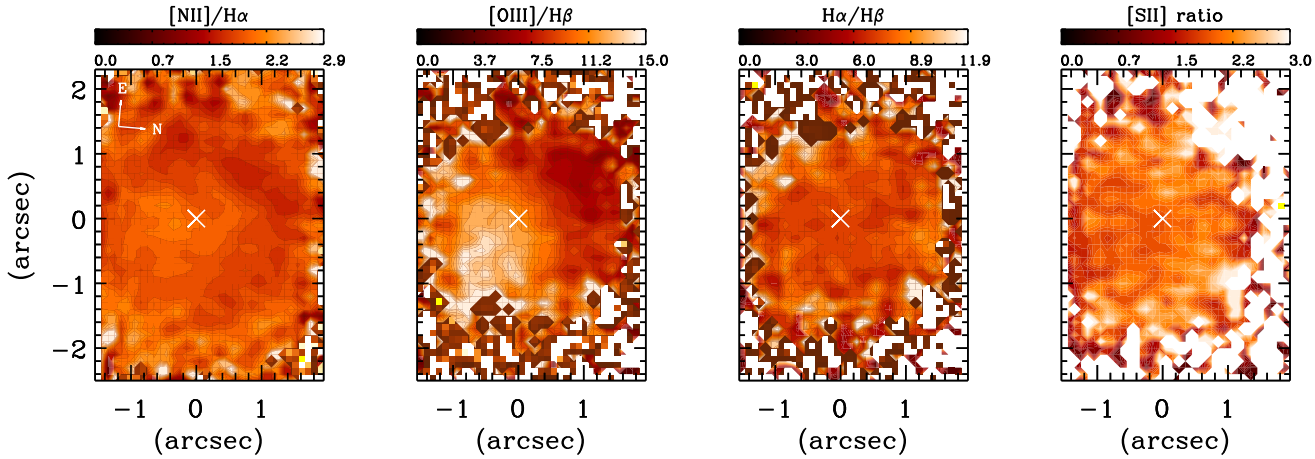

Figure 6. Maps of the line ratios [N II]/Hα, [O III]/Hβ, Hα/Hβ and [S II]6716/[S II]6730. Each panel follows the colour bar on top, and the white crosses mark the stellar kinematic centre.

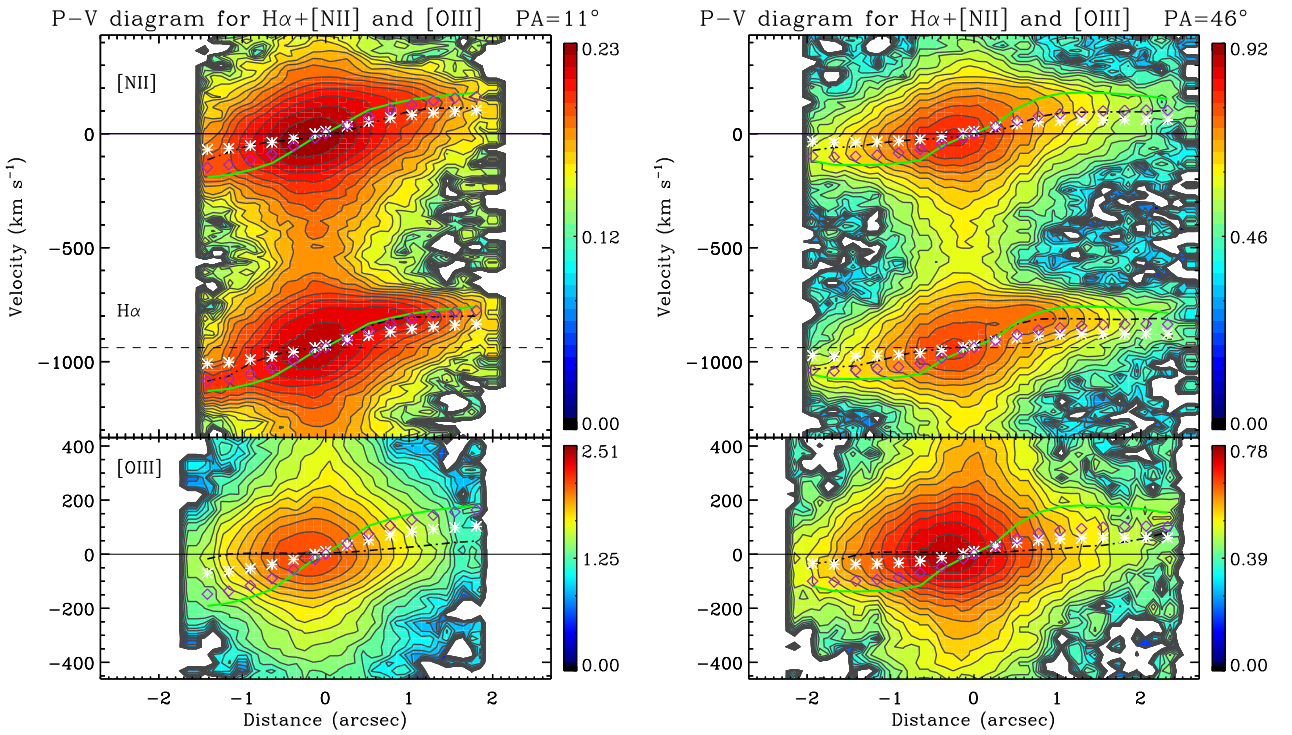

Figure 7. Position–velocity diagrams of the strongest emission lines: Hα + [N II] and [O III]. The PA of the simulated slit is indicated at the top of each set of panels (the major axis is at PA = 11°). The dashed–dot black lines show the velocities obtained from the single Gaussian fit, the solid green line represents the best bar-perturbation model (see Section 4), the purple diamonds correspond to the [N II] 'by-eye' rotation model, and the white asterisks are the stellar rotation model. The colour bars on the right of each panel have units of 10^{-15} erg cm^{-2} s^{-1} Å^{-1} arcsec^{-2}.

estimate the black hole mass via the central velocity dispersion:

$$\frac{M_{\rm BH}}{10^8\,{\rm M}_\odot} = (1.312 \pm 0.08)\left(\frac{\sigma}{200\ {\rm km\,s^{-1}}}\right)^{4.24\pm0.41}. \quad (2)$$

Using the summed spectrum of our data cube and PPXF, we find that the stellar velocity dispersion is 190 km s^{-1}, which implies a black hole mass of $M_{\rm BH} \approx (1.1 \pm 0.1) \times 10^8\,{\rm M}_\odot$ using equation (2).

We also estimated the accretion rate on to the black hole using

$$\dot{M}_{\rm acc} = \frac{L_{\rm bol}}{c^2\eta}, \quad (3)$$

where η is the conversion efficiency of the rest mass energy of the accreted material into radiation, typically assumed to be $\eta = 0.1$ for Seyfert galaxies (Frank, King & Raine 2002), and $L_{\rm bol}$ is the bolometric luminosity of the AGN. We follow Dumas et al. (2007) in using $L_{\rm bol} \approx 90 \times L_{\rm [O\,III]}$. The total [O III] luminosity in our FOV is $L_{\rm [O\,III]} = 3.5 \times 10^{41}$ erg s^{-1}, and thus $L_{\rm bol} \approx 3.1 \times 10^{43}$ erg s^{-1}.

Downloaded from https://academic.oup.com/mnras/article-abstract/489/3/4111/5571294 by Radboud University user on 23 October 2019

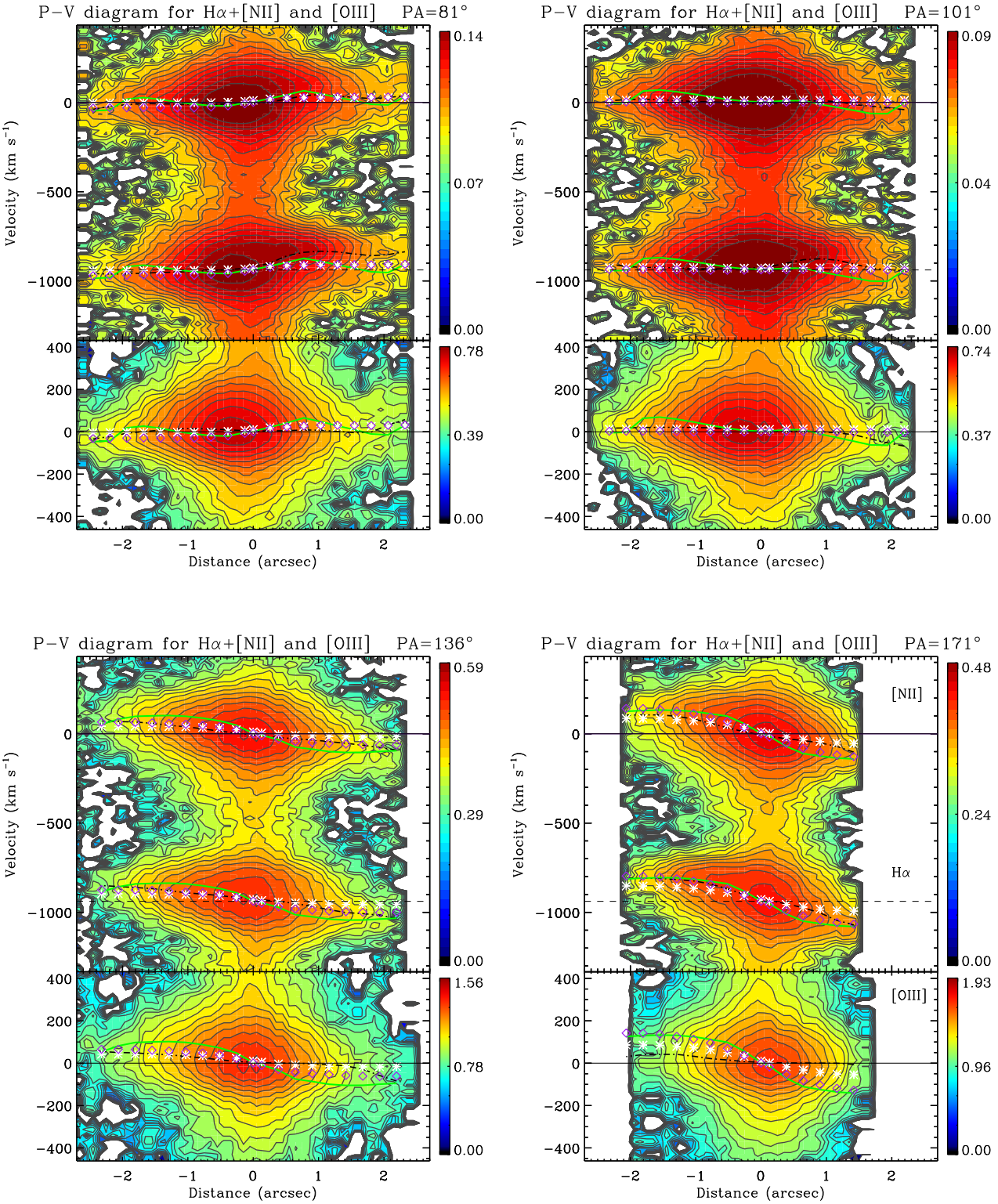

Figure 7 – *continued*

Substituting these values in equation (3), we estimate a mass accretion rate of $5.5 \times 10^{-3}\,\mathrm{M}_{\odot}\,\mathrm{yr}^{-1}$.

4 DISCUSSION

We have presented high-resolution stellar and ionized gas kinematics in the central kiloparsec of ESO 153-G20. Using single- and double-component Gaussian fits, P-V diagrams, and spectra over selected apertures, we have argued that two velocity components of ionized gas coexist in the central kiloparsec. One component rotates in (mostly) the same sense as the stars. This rotating gas component is clearly seen in all emission lines except [O III], where the two-component fit is required to tease out the weak rotating component.

Downloaded from https://academic.oup.com/mnras/article-abstract/489/3/4111/5571294 by Radboud University user on 23 October 2019

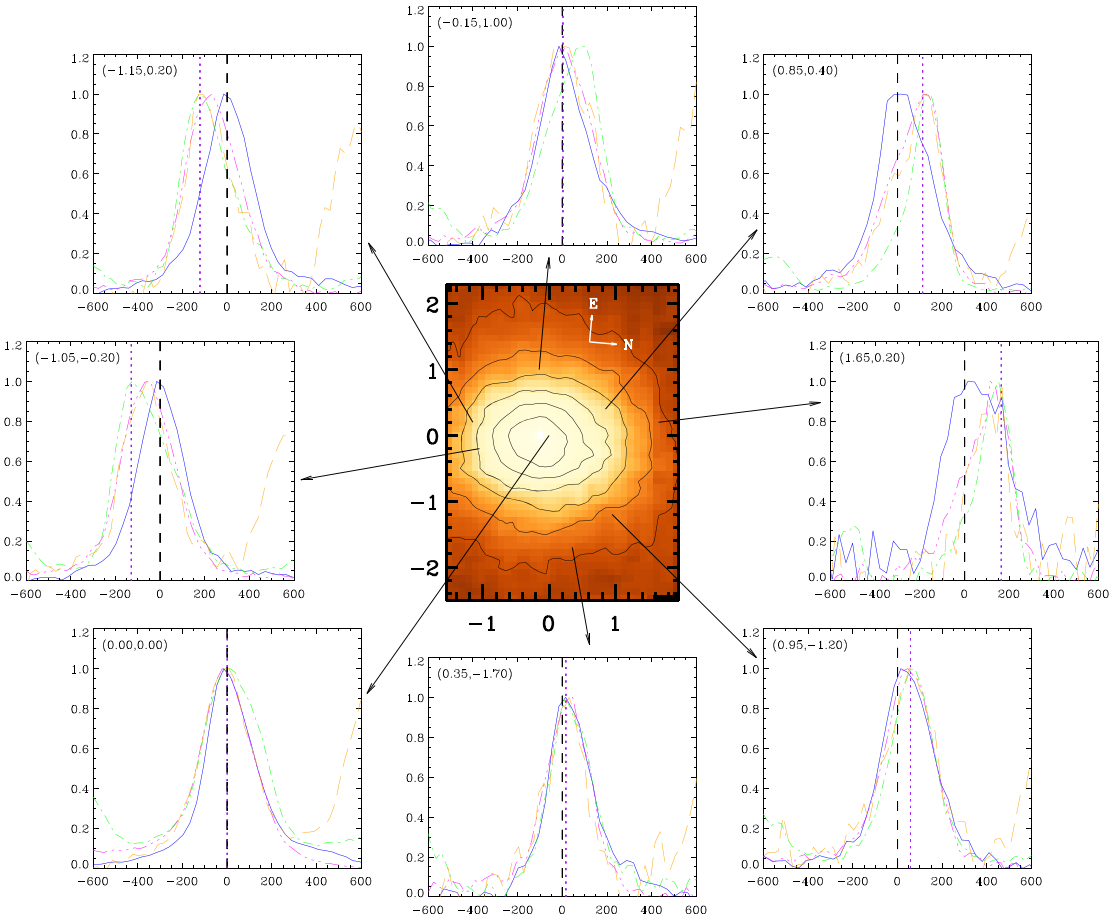

Figure 8. Normalized profiles for the [O III], Hα, [N II] and [S II] emission lines (in blue, green, magenta and orange, respectively; see text for details) in several 0.2-arcsec-radius apertures distributed across the FOV. The aperture position is indicated on the stellar continuum image and in each panel (as x and y offsets, in arcsec, from the nuclear position). The vertical black dashed line represents the systemic velocity of the galaxy (km s^{-1}), and the vertical purple dotted line corresponds to the velocity predicted from the [N II] 'by eye' rotation model (km s^{-1}). Spectra have been continuum-subtracted using the *continuum* task from IRAF.

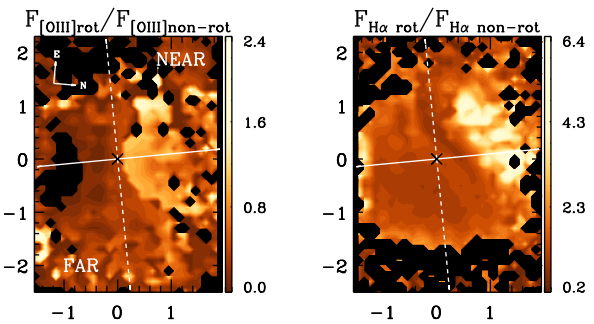

Figure 9. The ratio of total flux in the rotating component to total flux in the non-rotating, zero-velocity component for the two-component fit to the [O III] and Hα emission lines. Rotating gas dominates to the north-east, and the zero-velocity component dominates to the south-west.

The second component has a relatively large velocity dispersion (up to 125 km s^{-1}), and its velocity is consistent with the systemic velocity of the galaxy. While this component is seen in all emission lines, it is strongest in the [O III] line, and it is detected in a compact region centred at ∼0.25 arcsec south-west of the nucleus. A 2D Gaussian fit to the flux distribution of the non-rotating component in all emission lines gives a mean, almost circular, observed extent of 1.1 FWHM; after correcting for the seeing (FWHM ∼ 0.65), we obtained an intrinsic FWHM of ∼0.8 arcsec. The ionization state of the gas to the south-west of the nucleus, namely spatially coincident with this second component, is high, and the line ratios (e.g. [O III]/Hβ > 10, see Fig. 6) are AGN-like. As noted in Section 1, earlier *HST* imaging of the [O III] line suggested an ionization cone with PA ≈ −100° east of north (Schmitt et al. 2003). For these reasons, we interpret the zero-velocity component as gas in an ionization cone to the south-west of the nucleus. The detection of the He II λ4686 emission line at positions (1) and (2) (see Fig. 1) is a strong evidence of AGN photoionization and is also mainly seen in the region south-west of the nucleus (see Fig. 10).

The zero-velocity component is centred on the systemic velocity of the galaxy, and has a dispersion of ∼125 km s^{-1}. One interpretation is that the large line width comes from the intrinsic dispersion of gas, and not from any bulk velocity. However, it would be difficult to explain such a large dispersion in a compact off-nuclear region. Alternatively, the gas is outflowing from the nucleus and lit up by the ionizing radiation. In this case, the ionization cone would have its axis along the plane of the sky, in order to give a central velocity centred on systemic. Projection effects (given a large opening angle of the cone) and/or acceleration/deceleration along the 0.8-arcsec extent creates the observed line width. The locations of the posited ionization cone to the south-west and the equivalent position to

Downloaded from https://academic.oup.com/mnras/article-abstract/489/3/4111/5571294 by Radboud University user on 23 October 2019

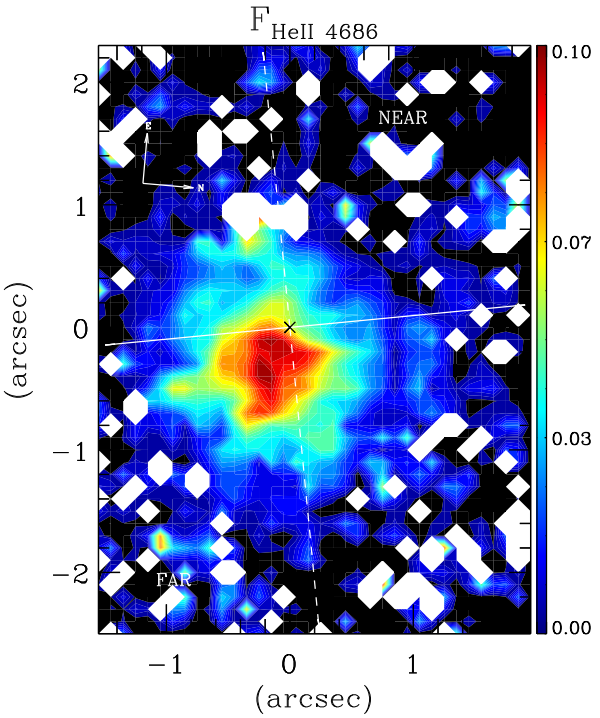

Figure 10. Flux distribution of the He II emission line. Units are in 10^{-15} erg cm^{-2} s^{-1} Å^{-1} arcsec^{-2}. The panel follows the colour bar on its right, and the axes (in arcsec) are relative to the stellar kinematic centre indicated by the black cross. The solid (dashed) line indicates the major (minor) axis. The near and far sides of the disc are indicated.

the north-east where we would expect the counter-cone are marked with red circles in the structure map (Fig. 1). Clearly, the predicted location of the counter-cone is coincident with a strong dust lane seen on the near side of the galaxy disc. Extinction resulting from this dust lane would explain the lack of detection of the counter-cone.

The interpretation of an ionization cone to the south-west with an obscured counter-cone to the north-east is supported by the dispersion seen in the Hα and Hβ lines (Section 3.2.1). The visible ionization cone to the south-west contributes to the Hα and Hβ emission profiles. This, together with the rotating gas component in these lines, produces high-velocity dispersions to the south-west. Because the north-east ionization cone is obscured, the Hα and Hβ dispersions to the north-east reflect only the dispersion of the rotating component and thus, the values in this direction are lower. The higher value of 'dispersion' seen towards the nucleus can be explained as being due to the high (solid-body) rotation-curve gradient in this region. Dust in the nucleus would also explain the offset between the kinematic centre and the radius at which the south-west ionization cone is first detected ($\sim$ 96 pc). To fully obscure the counter-cone by the near side of the galaxy then requires that the half-opening angle of the cone is $\leq 40^\circ$, given that the galaxy disc has an inclination of 51°. This value is in agreement with the opening angle derived by Schmitt et al. (2003). If an opening angle of 40° is assumed, then the line width of the zero-component would imply that the true outflow velocity is $v \approx 400$ km s^{-1}, although this would be higher if a smaller opening angle were used.

An alternative explanation for the high velocities seen in the second component is an outflow produced by an off-nuclear starburst. We extracted aperture spectra from the two regions marked with the red circles in the structure map (Fig. 1), namely the locations of the posited ionization cone and the unseen counter-cone. Fits to these two spectra with pPXF show that the stellar templates used in both cases are very similar in terms of stellar population ages. That is, while both require a relatively large fraction of young stars, there is no strong evidence that one is significantly younger than the other. González Delgado, Heckman & Leitherer (2001) studied the relation of gas excitation and starburst processes in a sample of 20 Seyfert 2 galaxies by analysing their near-ultraviolet (looking for high-order terms of the Balmer series in absorption) and optical spectra, focusing on the nuclear and circumnuclear regions. They found that the nuclei of starburst spiral galaxies have a very low excitation ([O III]/H$\beta \leq 1$), which is not the case for the galaxy that we are studying. For these reasons, and because of the evidence of AGN photoionization presented above, we disfavour a starburst origin for the zero-velocity component.

Assuming that the zero-velocity component represents outflowing gas with deprojected velocity $v \approx 400$ km s^{-1} along the ionization cone, we estimated the mass outflow rate as the ratio between the mass of the outflowing gas and the dynamical time at the nucleus (M_g/t_d). We derived the gas mass as

$$M_g = N_e m_p V f, \tag{4}$$

where N_e is the electron density, m_p is the mass of a proton, V is the volume of the region where the outflow is detected, and f is the filling factor, which can be estimated from

$$L_{H\alpha} \sim f N_e^2 j_{H\alpha}(T) V, \tag{5}$$

where $j_{H\alpha}(T) = 3.534 \times 10^{-25}$ erg cm^{-3} s^{-1} (Osterbrock 1989) and $L_{H\alpha}$ is the Hα luminosity emitted by a volume V.

Substituting equation (5) into equation (4), we obtain

$$M_g = \frac{m_p L_{H\alpha}}{N_e j_{H\alpha}(T)}. \tag{6}$$

Considering a luminosity distance of 80.7 Mpc, the Hα luminosity derived from the whole FOV ($L_{H\alpha} \approx 2.3 \times 10^{41}$ erg s^{-1}), and $N_e = 960$ cm^{-3} (the mean value for the electron density within the inner 0.8 arcsec centred on the outflow peak), we obtain $M_g \approx 6 \times 10^5$ M$_\odot$. From the double Gaussian fit we performed in selected apertures (see Section 3.2.2), we concluded that almost 70 per cent of the Hα emission comes from the non-rotating component, that is, from a mass of $\sim 4 \times 10^5$ M$_\odot$. The dynamical time can be estimated from the ratio between the extent of the region over which we detect the outflow (0.8 arcsec $\approx$ 308 pc) and the velocity of the outflow (taken to be $\sim$400 km s^{-1}). This gives $t_d \approx 7.5 \times 10^5$ yr, and thus the mass outflow rate is $\dot{M}_{out} \sim 5.4 \times 10^{-1}$ M$_\odot$ yr^{-1}. This value should then be doubled, $\dot{M}_{out} \sim 1.1$ M$_\odot$ yr^{-1}, to account for the second, invisible, ionization cone. This outflow rate is $\sim$200 times the estimated accretion rate on to the SMBH in ESO 153-G20 (Section 3.3).

We also estimated the kinetic power of the outflow using the expression from section 4.2 in Humire et al. (2018). However, we neglected the velocity dispersion term. This is because of the difficulties in separating the multiple components: we cannot distinguish what fraction of the total line width comes from bulk velocity projection effects or from intrinsic dispersion in the gas (although the former is likely to dominate). We derived a kinetic power of $\dot{E}_{out} = 5.4 \times 10^{40}$ erg s^{-1}. Comparing this with the bolometric luminosity ($L_{bol} = 3.1 \times 10^{43}$ erg s^{-1}; Section 3.3), we obtain $\dot{E}_{out}/L_{bol} \approx 1.7 \times 10^{-3}$.

Another notable kinematic feature is the presence of S-shaped isovelocity contours in the gas velocity maps, most prominent in the Hα and [N II] emission lines. These features are often seen in barred

Downloaded from https://academic.oup.com/mnras/article-abstract/489/3/4111/5571294 by Radboud University user on 23 October 2019

galaxies, and have been explained as perturbations produced by the bar (Bosma 1978; Schommer et al. 1988; Moore & Gottesman 1998; Combes et al. 2002; Fuentes-Carrera et al. 2019). Because ESO 153-G20 shows clear evidence of a bar (RC3; Schmitt & Kinney 2000) we briefly explore the kinematic signature expected using the linear perturbation analysis outlined in Finlez et al. (2018). Briefly, then, this procedure starts with an unperturbed rotation curve based on the mass of the galaxy disc, the photometric parameters of the galaxy (disc and bar PAs, and bar ellipticity) and uses linear perturbation analysis (Wong, Blitz & Bosma 2004; Fathi et al. 2005; van de Ven & Fathi 2010) to predict the velocity field expected for different values of bar pattern speed and 'damping' (which simulates a radial frictional force). We thus first created an unperturbed velocity field, based on an exponential disc with a total disc mass of $M_{\rm d} = 1 \times 10^{11}$ M$_\odot$ and a disc scale-length of $r_{\rm d} = 1$ kpc. This initial configuration did not converge properly to a solution owing to the fact that our kinematical centre is not located at the geometric centre of the image. Because of this issue, we chose 'by eye' the values of $M_{\rm d}$ and $r_{\rm d}$ by comparison with the Hα velocity field, obtaining $M_{\rm d} = 1.2 \times 10^{10}$ M$_\odot$ and $r_{\rm d} = 0.46$ kpc. We assumed $PA_{\rm disc} = 11^\circ$, $PA_{\rm bar} = 126^\circ$ (as obtained from the *I*-band image in Schmitt & Kinney 2000), and a bar ellipticity $\epsilon = 0.4$ (the mean value obtained by modelling the WFPC2-*HST* image from Fig. 1 with GALFIT, Peng et al. 2002, and DISKFIT, Spekkens & Sellwood 2007; Sellwood & Sánchez 2010). We perturbed this model, creating a matrix of velocity fields by varying the bar-pattern speed ($\Omega_{\rm p}$) over the range 20 to 300 km s^{-1} kpc^{-1} and the damping factor (λ) over the range 0.01 to 0.4.

None of the perturbed models exactly reproduces the S-shaped kinematic pattern seen in the Hα and [N II] emission lines. We therefore did not proceed to the next step of minimizing residuals and thus determining the best-fitting bar-perturbation model and its associated parameters. However, some of the perturbed maps did produce roughly the kinematic morphology observed. We show four examples of these 'roughly matching' bar-perturbed models in Fig. 11. Of the four, the one with $\Omega_{\rm p} = 250$ and $\lambda = 0.07$ most closely resembles the observed velocity field, and we plotted its predicted velocities in the P-V diagrams in Section 3.2.2. Effectively, while we cannot exactly reproduce the distortions in the rotating component of the emission-line gas, it is most likely that these are due to perturbations induced by the bar. Unfortunately, this complication means that we are unable to further analyse the rotation-component velocity field for signatures of streaming inflows. The major limiting factor in this analysis is the modest extent of our FOV.

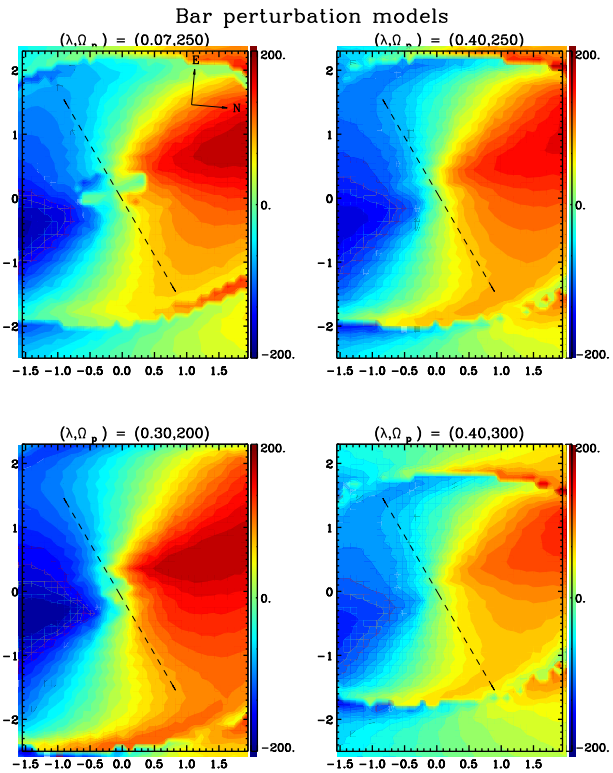

Figure 11. Example velocity field models obtained by adding 'bar-perturbations' to an axisymmetric rotation curve. The bar and disc PA, bar ellipticity, and disc mass were fixed to values measured for ESO153-G20, while the bar-pattern speed ($\Omega_{\rm p}$) and damping factor (λ) were varied (see text). Each panel lists the values of $\Omega_{\rm p}$ (in km s^{-1}kpc^{-1}) and λ, and its colours follow the bar on the right. We show only four selected models, which are the most reminiscent of the observed velocity fields. The dashed line shows the PA of the bar (126°).

5 CONCLUSIONS

We have observed the inner 1.4 × 1.9 kpc^2 of the Seyfert 2 galaxy ESO 153-G20 using the GMOS integral field spectrograph on the Gemini South Telescope, at a spatial resolution of $\Delta_{\rm r} \approx 250$ pc and covering the wavelength range 4110–7280 Å at a spectral resolution of $\sigma_{\rm inst} \approx 36$ km s^{-1}. This allowed the detection of prominent emission lines (Hβ, [O III] $\lambda\lambda$4959, 5007, Hα + [N II] $\lambda\lambda$6548, 6583, [S II] $\lambda\lambda$6716, 6731), and the derivation of the gaseous and stellar kinematics. One- and two-component Gaussian fits, aperture spectra, and P-V diagrams were used to obtain spatially resolved fluxes, radial velocities and velocity dispersions, and to analyse the kinematics. The main results are as follows.

(i) The stellar velocity field traces circular rotation with the line of nodes oriented at PA ≈ 11° and reaching amplitudes of ± 96 km s^{-1}.

(ii) Dust obscuration seen in the structure map and the assumption of trailing spiral arms indicate that the near side of the galaxy disc is to the east.

(iii) Single and double Gaussian fits, aperture spectra, and P-V diagrams reveal that all emission lines have two kinematic components: a rotating component that follows the stellar kinematics, and a higher-dispersion zero-velocity component, with its brightest emission seen as a 0.8-arcsec (308-pc) diameter region centred at a projected distance of 0.25 arcsec (∼96 pc) south-west of the nucleus. We interpret this region as due to an outflow observed along an ionization cone in the plane of the sky.

(iv) High [O III]/Hβ ratios (>10) are seen towards the region in which most of the zero-velocity component is found, consistent also with gas illuminated by an AGN ionization cone. The equivalent aperture on the other side of the nucleus shows significantly lower values (<4), indicating emission from gas with lower excitation. In fact, this latter aperture falls on a prominent dust lane on the near side of the galaxy disc. We speculate that the compact counter-cone is obscured by this dust lane, and that the base of the visible ionization cone is also obscured by dust.

(v) Given that the velocity of the outflowing component is close to zero (systemic velocity), and that the counter-cone seems to be behind the galaxy plane on its east side, we posit that the ionization cone has an axis in the plane of the sky and a half-opening angle of ≤ 40°. The outflowing gas has bulk velocity $v \approx 400$ km s^{-1} along

Downloaded from https://academic.oup.com/mnras/article-abstract/489/3/4111/5571294 by Radboud University user on 23 October 2019

the ionization cones, and the line width is produced primarily by projection effects.

(vi) Assuming a bi-conical outflow, with one side invisible owing to obscuration, a mass outflow rate $\dot{M}_{\rm out} \approx 1.1\ {\rm M}_{\odot}\ {\rm yr}^{-1}$ is obtained for ESO 153-G20. This value is significantly higher (∼200 times) than the accretion rate necessary to support the AGN luminosity.

(vii) Perturbations produced by the bar are a likely explanation for the S-shape observed in the Hα velocity field, although our linear perturbation models fail to exactly reproduce this S-shape.

ACKNOWLEDGEMENTS

This work is based on observations obtained at the Gemini Observatory, which is operated by the Association of Universities for Research in Astronomy, Inc., under a cooperative agreement with the NSF on behalf of the Gemini partnership: the National Science Foundation (USA), National Research Council (Canada), CONICYT (Chile), Ministerio de Ciencia, Tecnología e Innovación Productiva (Argentina), Ministério da Ciência, Tecnologia e Inovação (Brazil), and Korea Astronomy and Space Science Institute (Republic of Korea). NN acknowledges support from Conicyt (PIA ACT172033, Fondecyt 1171506 and BASAL AFB-170002). RAR acknowledges support from FAPERGS (project no. 16/2551-0000251-7) and CNPq (project N0. 303373/2016-4). DM gratefully acknowledges support from CONICYT-PFCHA/Doctorado Nacional/2019-21191543.

REFERENCES

Allington-Smith J. et al., 2002, PASP, 114, 892
Begelman M. C., Blandford R. D., Rees M. J., 1984, Rev. Mod. Phys., 56, 255
Bertola F., Bettoni D., Danziger J., Sadler E., Sparke L., de Zeeuw T., 1991, ApJ, 373, 369
Bosma A., 1978, PhD thesis, Groningen University
Buta R., 1995, ApJS, 96, 39
Buta R., Crocker D. A., 1991, AJ, 102, 1715
Buta R., Crocker D. A., 1993, AJ, 105, 1344
Cappellari M., 2017, MNRAS, 466, 798
Cappellari M., Copin Y., 2003, MNRAS, 342, 345
Cappellari M., Emsellem E., 2004, PASP, 116, 138
Combes F., Boisse P., Mazure A., Blanchard A., Seymour M., 2002, Galaxies and Cosmology. Springer, New York
Combes F. et al., 2013, A&A, 558, A124
da Costa L. N., Pellegrini P. S., Davis M., Meiksin A., Sargent W. L. W., Tonry J. L., 1991, ApJS, 75, 935
Davies R. I., Maciejewski W., Hicks E. K. S., Tacconi L. J., Genzel R., Engel H., 2009, ApJ, 702, 114
de Grijp M. H. K., Lub J., Miley G. K., 1987, A&AS, 70, 95
de Vaucouleurs G., de Vaucouleurs A., Corwin H. G., Jr, Buta R. J., Paturel G., Fouqué P., 1991, Third Reference Catalogue of Bright Galaxies. Volume I: Explanations and References. Volume II: Data for Galaxies between 0^h and 12^h. Volume III: Data for Galaxies between 12^h and 24^h. Springer, New York
Dumas G., Mundell C. G., Emsellem E., Nagar N. M., 2007, MNRAS, 379, 1249
Emsellem E., Fathi K., Wozniak H., Ferruit P., Mundell C. G., Schinnerer E., 2006, MNRAS, 365, 367
Englmaier P., Shlosman I., 2004, ApJ, 617, L115
Erwin P., Sparke L. S., 1999, ApJ, 512, L37
Falcón-Barroso J., Sánchez-Blázquez P., Vazdekis A., Ricciardelli E., Cardiel N., Cenarro A. J., Gorgas J., Peletier R. F., 2011, A&A, 532, A95
Fathi K., Storchi-Bergmann T., Riffel R. A., Winge C., Axon D. J., Robinson A., Capetti A., Marconi A., 2006, ApJ, 641, L25
Fathi K., van de Ven G., Peletier R. F., Emsellem E., Falcón-Barroso J., Cappellari M., de Zeeuw T., 2005, MNRAS, 364, 773
Finlez C., Nagar N. M., Storchi-Bergmann T., Schnorr-Müller A., Riffel R. A., Lena D., Mundell C. G., Elvis M. S., 2018, MNRAS, 479, 3892
Frank J., King A., Raine D. J., 2002, Accretion Power in Astrophysics, 3rd edn. Cambridge University Press, Cambridge, UK
Freitas I. C. et al., 2018, MNRAS, 476, 2760
Fuentes-Carrera I. et al., 2019, A&A, 621, A25
García-Burillo S. et al., 2015, A&A, 580, A35
García-Burillo S. et al., 2017, A&A, 608, A56
González Delgado R. M., Heckman T., Leitherer C., 2001, ApJ, 546, 845
Gültekin K. et al., 2009, ApJ, 698, 198
Hamuy M., Suntzeff N. B., Heathcote S. R., Walker A. R., Gigoux P., Phillips M. M., 1994, PASP, 106, 566
Hamuy M., Walker A. R., Suntzeff N. B., Gigoux P., Heathcote S. R., Phillips M. M., 1992, PASP, 104, 533
Hook I. M., Jørgensen I., Allington-Smith J. R., Davies R. L., Metcalfe N., Murowinski R. G., Crampton D., 2004, PASP, 116, 425
Humire P. K. et al., 2018, A&A, 614, A94
Kauffmann G. et al., 2003, MNRAS, 346, 1055
Kewley L. J., Groves B., Kauffmann G., Heckman T., 2006, MNRAS, 372, 961
Knapen J. H., 2005, Gravitationally Induced Inflow in Starbursts and AGN. Springer Netherlands, Dordrecht, p. 85
Kormendy J., Ho L. C., 2013, ARA&A, 51, 511
Krajnović D., Cappellari M., de Zeeuw P. T., Copin Y., 2006, MNRAS, 366, 787
Krist J. E., Hook R. N., Stoehr F., 2011, Proceedings of the SPIE, 20 years of Hubble Space Telescope optical modeling using Tiny Tim. p. 81270J
Lauberts A., 1982, ESO/Uppsala Survey of the ESO(B) Atlas. European Southern Observatory (ESO), Garching
Lauberts A., Valentijn E. A., 1989, The Surface Photometry Catalogue of the ESO-Uppsala Galaxies, European Southern Observatory (ESO), Garching
Lena D., Robinson A., Storchi-Bergmann T., Couto G. S., Schnorr-Müller A., Riffel R. A., 2016, MNRAS, 459, 4485
Lena D. et al., 2015, ApJ, 806, 84
Lynden-Bell D., 1969, Nature, 223, 690
Moore E. M., Gottesman S. T., 1998, MNRAS, 294, 353
Muñoz-Vergara D. et al., 2019, MNRAS, 487, 3679
Osterbrock D. E., 1989, Astrophysics of Gaseous Nebulae and Active Galactic Nuclei. University Science Books, USA
Paturel G., Petit C., Prugniel P., Theureau G., Rousseau J., Brouty M., Dubois P., Cambrésy L., 2003, A&A, 412, 45
Peng C. Y., Ho L. C., Impey C. D., Rix H.-W., 2002, AJ, 124, 266
Pogge R. W., Martini P., 2002, ApJ, 569, 624
Ramakrishnan V. et al., 2019, MNRAS, 487, 444
Repetto P., Faúndez-Abans M., Freitas-Lemes P., Rodrigues I., de Oliveira-Abans M., 2017, MNRAS, 464, 293
Riffel R. A., 2010, Ap&SS, 327, 239
Riffel R. A., Storchi-Bergmann T., Riffel R., 2015, MNRAS, 451, 3587
Rosario D. J., Whittle M., Nelson C. H., Wilson A. S., 2010, MNRAS, 408, 565
Sarzi M., Rix H.-W., Shields J. C., Ho L. C., Barth A. J., Rudnick G., Filippenko A. V., Sargent W. L. W., 2005, ApJ, 628, 169
Schmitt H. R., Donley J. L., Antonucci R. R. J., Hutchings J. B., Kinney A. L., 2003, ApJS, 148, 327
Schmitt H. R., Kinney A. L., 2000, ApJS, 128, 479
Schnorr-Müller A., Storchi-Bergmann T., Nagar N. M., Ferrari F., 2014b, MNRAS, 438, 3322
Schnorr-Müller A., Storchi-Bergmann T., Nagar N. M., Robinson A., Lena D., Riffel R. A., Couto G. S., 2014a, MNRAS, 437, 1708
Schnorr Müller A., Storchi-Bergmann T., Riffel R. A., Ferrari F., Steiner J. E., Axon D. J., Robinson A., 2011, MNRAS, 413, 149
Schommer R. A., Caldwell N., Wilson A. S., Baldwin J. A., Phillips M. M., Williams T. B., Turtle A. J., 1988, ApJ, 324, 154
Sellwood J. A., Sánchez R. Z., 2010, MNRAS, 404, 1733
Shlosman I., Begelman M. C., Frank J., 1990, Nature, 345, 679

Downloaded from https://academic.oup.com/mnras/article-abstract/489/3/4111/5571294 by Radboud University user on 23 October 2019

Simões Lopes R. D., Storchi-Bergmann T., de Fátima Saraiva M., Martini P., 2007, ApJ, 655, 718
Skrutskie M. F. et al., 2006, AJ, 131, 1163
Slater R. et al., 2019, A&A, 621, A83
Spekkens K., Sellwood J. A., 2007, ApJ, 664, 204
Storchi-Bergmann T., Dors O. L., Jr., Riffel R. A., Fathi K., Axon D. J., Robinson A., Marconi A., Östlin G., 2007, ApJ, 670, 959
Sánchez-Blázquez P. et al., 2006, MNRAS, 371, 703
van de Ven G., Fathi K., 2010, ApJ, 723, 767
van Dokkum P. G., Bloom J., Tewes M., 2012, L.A.Cosmic: Laplacian Cosmic Ray Identification. Astrophysics Source Code Library, record ascl:1207.005
Vazdekis A., Sánchez-Blázquez P., Falcón-Barroso J., Cenarro A. J., Beasley M. A., Cardiel N., Gorgas J., Peletier R. F., 2010, MNRAS, 404, 1639
Wong T., Blitz L., Bosma A., 2004, ApJ, 605, 183

This paper has been typeset from a TEX/LATEX file prepared by the author.

Downloaded from https://academic.oup.com/mnras/article-abstract/489/3/4111/5571294 by Radboud University user on 23 October 2019